

**Modeling the Formation of
Iron Sulfide Scales**

Using Thermodynamic Simulation Software

Andrzej Anderko

**OLI Systems Inc.
108 American Road, Morris Plains, NJ
07950, USA**

Patrick J. Shuler

**Chevron Petroleum Technology Company
1300 Beach Boulevard
La Habra, CA 90631**

1998

Modeling the Formation of Iron Sulfide Scales Using Thermodynamic Simulation Software

Andrzej Anderko
OLI Systems Inc.
108 American Road
Morris Plains, NJ 07950

Patrick J. Shuler
Chevron Petroleum Technology Company
1300 Beach Boulevard
La Habra, CA 90631

Abstract

A program has been developed for generating stability diagrams that concisely represent the thermodynamic state of multicomponent, multiphase aqueous systems in wide ranges of temperature and component concentrations. The diagrams are based on a thermodynamic model that combines the Helgeson-Kirkham-Flowers equation of state for standard-state properties with a solutions nonideality model based on the activity coefficient expressions developed by Bromley and Pitzer. The diagrams offer a flexible choice of independent variables, which include component concentrations in addition to the potential and pH. The stability diagrams are used to predict the conditions that favor the formation of stable and metastable iron sulfide species, which are commonly deposited under oil field-related conditions. First, the diagrams have been applied to establish a sequence of transformations that iron sulfides undergo as they age. The predicted transformation sequences take into account environmental variables (e.g., hydrogen sulfide concentration, oxygen availability, etc.). The predictions are in agreement with experimental data on iron sulfide formation at the iron/solution interface and in bulk solution. The understanding of iron sulfide transformation sequences makes it possible to simulate experimental studies of H₂S/CO₂ corrosion in the presence or absence of oxygen. A comparison with laboratory corrosion rate data under gas pipeline conditions indicates that the magnitude of corrosion rates can be correlated with the predicted stability of metastable iron sulfide phases.

KEY WORDS: H₂S corrosion, iron sulfides, thermodynamics, speciation, stability diagrams, software

Introduction

Iron sulfide scales are frequently formed under oil field-related conditions as a result of deposition from produced water or corrosion of steels in CO₂/H₂S environments. The formation of iron sulfides is complicated by the existence of several stable and metastable Fe-S compounds. They are produced as a result of complex, both chemically and biologically mediated, reactions and undergo various transformations as they age. The stability of various iron sulfides depends on conditions such as pH, availability of oxygen, concentration of sulfur-bearing species, composition of the aqueous electrolyte environment and mechanism of biological activity. The chemical identity of the deposited Fe-S species influences corrosion rates at the interface between iron or steel and H₂S-containing aqueous environments. Evidence exists that various iron sulfides form natural sequences in developing corrosion

products^{1,2}. These sequences are, to a large extent, analogous to the transformations in a wide variety of geochemical settings³⁻⁸. Therefore, it is worthwhile to develop modeling techniques to elucidate the conditions under which the stable and metastable iron sulfides can be formed.

Thermodynamic properties of iron sulfides determine their formation as a result of corrosion of iron and their subsequent transformations. Therefore, thermodynamic stability analysis can serve as a useful tool for analyzing the stability of various Fe-S compounds. Although thermodynamic calculations do not reveal the mechanism of the formation of individual species, they make it possible to find their relative stability. In turn, the relative stability of intermediate species can be used to predict the transformations of various Fe-S compounds as they age. For example, if thermodynamic stability analysis reveals that a precursor A is less stable than an intermediate product B, which is less stable than a final product C, then a transformation $A \rightarrow B \rightarrow C$ is likely to occur.

As a convenient tool for such analysis, a program has been developed for generating real-solution stability diagrams⁹, which combine the ease-of-use of the Pourbaix¹⁰ diagrams with a realistic model of multicomponent, nonideal aqueous solutions. The diagrams indicate under which conditions the solids of interest are stable and which conditions may cause their dissolution or transformation into other solid phases. In this study, we describe the program for generating the real-solution stability diagrams and demonstrate its usefulness for predicting the formation of both stable and metastable iron sulfides. The predictions are further used to establish theoretical replacement sequences, which can be compared with experimental results. Finally, the stability diagrams are used to find relationships between the stability of iron sulfides and corrosion rates observed in laboratory studies of $\text{CO}_2/\text{H}_2\text{S}$ corrosion in the presence or absence of oxygen.

Structure of the Program

The stability diagrams are generated using the CSP Stability program, which is a part of OLI Systems' CSP software package¹¹. The computations are based on a realistic thermodynamic model that combines information about standard-state properties of all species of interest with a formulation for the excess Gibbs energy, which accounts for solution nonideality. This model has been described in detail by Zemaitis et al.¹² and Rafal et al.¹³ Here, the essential elements of the model are summarized in the Appendix. The model is coupled with an algorithm for calculating phase equilibria in multicomponent systems that may contain an aqueous phase, any number of solid phases and, if necessary, a vapor and a nonaqueous liquid phase. The combined thermodynamic model is valid for temperatures up to 300 °C, pressures up to 1 kbar and compositions up to 30 mol/kg.

The overall structure of the program is outlined in Figure 1. As shown in Figure 1, the software utilizes a comprehensive data bank, which contains thermodynamic properties of aqueous, solid and gaseous species. In particular, the following properties are stored for distinct chemical species:

- (1) Reference-state thermochemical properties, i.e., the Gibbs energy and enthalpy of formation, entropy, heat capacity and volume;
- (2) Parameters of the Helgeson-Kirkham-Flowers equation of state^{14,15} for standard-state thermodynamic properties as functions of temperature and pressure;
- (3) Interaction parameters for the Bromley¹⁶ and Pitzer¹⁷ liquid-phase activity coefficient models;

- (4) Parameters that are used to calculate the properties of the gas phase from the Soave¹⁸ equation of state;
- (5) A set of independent reactions that the species may undergo; these reactions may involve oxidation-reduction, complexation, acid-base transformations and precipitation.

In the first step, the user defines the solutes that exist in the considered system. Then, the software utilizes the information stored in the data bank to generate an aqueous chemistry model. In the chemistry model, all possible species in the system are enumerated and their properties are retrieved from the data bank. This provides a full speciation of the system, including both ionic and neutral species in the aqueous phase and all possible solid phases.

In the second step, thermodynamic conditions are defined for the thermodynamic simulation. These conditions include temperature, pressure and the overall concentrations of solutes. In the third step, the stability diagram is defined by specifying the independent variables, their ranges and titrants that are used to change the independent variables. In general, two kinds of diagrams can be generated, i.e.,

- (1) Electrochemical diagrams, i.e., those utilizing the potential (E) and pH or concentrations of aqueous species as independent variables. These diagrams are extensions of the classical Pourbaix¹⁰ diagrams to real (e.g., concentrated) solutions. They have been described in detail by Anderko et al.⁹. These diagrams make it possible to analyze various combinations of redox processes on metal surfaces that may lead to the formation of potentially protective films or to the dissolution of metals. In this study, these diagrams will be used to find the replacement sequence of iron sulfide phases that undergo transformations as they age.
- (2) Chemical diagrams, i.e., those utilizing concentrations of various species and/or temperature as independent variables. The potential is not an independent variable but, rather, results from the solution of chemical and phase equilibria in the system of interest. These diagrams show the most stable species in the system and, thus, represent the global equilibrium of the system. In this work, these diagrams will be used to simulate laboratory experiments in which the amounts of reactants such as H₂S, CO₂ or O₂ are varied in addition to pH.

Also, redox subsystems that will be considered in the simulations are defined at this stage. A redox subsystem contains all species of a given element in various oxidation states. For the study of iron sulfides, it is necessary to consider simultaneously iron and sulfur in various oxidation states.

As shown in Figure 1, these three kinds of information (i.e., the chemistry model, thermodynamic conditions and diagram specifications) are further used to perform equilibrium thermodynamic computations. If pH is of interest as an independent variable, thermodynamic computations are repeatedly performed to cover the full range of pH. To vary the pH, calculations are performed with changing amounts of H₂SO₄ and NaOH, which are used as titrants. Usually, 25-40 equilibrium calculations with varying amounts of acidic and basic titrants are required. If concentrations of selected species (e.g., H₂S or O₂) are used as independent variables, they are varied within predetermined ranges. The computations provide the equilibrium activities of all species as functions of independent variables. Finally, stability diagrams are constructed using the calculated activities and information on the chemical structure, oxidation states, stoichiometry and charges of all species in the chemical speciation model. Algorithms for constructing stability diagrams based on these data have been described in detail by Anderko et al.⁹ and Lencka et al.¹⁹ for the electrochemical and chemical diagrams, respectively.

Results and Discussion

Replacement Sequence of Iron Sulfides

In this study, stability diagrams are utilized to simulate the formation of both stable and metastable species. To predict the replacement sequence of solids during their aging, stability diagrams are first generated with all possible species taken into account. This shows the most stable species in their stability fields. Then, selected stable species are excluded and the diagrams are generated again to reveal which species are next in the order of thermodynamic stability. Such species are likely to act as precursors of the more stable species. This process can be repeated several times to find a complete replacement sequence for compounds that undergo changes as they age. This approach is quite general and can be applied to any family of compounds that exhibit transformations between metastable and stable species. In this work, this method is used for predicting the replacement sequence of iron sulfides.

The Fe-S species that were considered in the simulations are collected in Table 1 together with their thermochemical properties. The stoichiometry of amorphous iron sulfide and mackinawite was assumed to be FeS and, therefore, no stoichiometric variations were allowed. This assumption was necessary to maintain consistency with the thermochemical data of Berner³, which were obtained for stoichiometric compounds. For some species (i.e., mackinawite, greigite, amorphous FeS and FeHS⁺), only Gibbs energies of formation were available from experimental data. In these cases, the entropies were estimated from Latimer's²⁰ contributions and heat capacities were calculated using the method of Kubaschewski and Ünal²¹.

The simulations were performed for iron sulfides formed in a brine with a composition given in Table 2 at $t = 25\text{ }^{\circ}\text{C}$ and $P = 1\text{ bar}$. The composition given in Table 2 is an average for the produced water fluids at an oil field located in Colorado. The pH of this brine is 6.5. Brines of this composition are of practical interest because iron sulfides frequently precipitate from produced water in oil wells. The results of simulations are shown in Figures 2-6. The names of the species in Figs. 2-6 contain the suffixes -PPT, -ION and -AQ, which denote solids (or precipitates), ions and neutral aqueous species, respectively. When necessary, the symbols of elements are followed by Roman numerals denoting their oxidation states. For example, FEIIIION and FEIIOH3ION denote the Fe(III)³⁺ and Fe(II)(OH)₃⁻ ions, respectively.

Figure 2 shows the stability diagram when all possible Fe-S species are considered. Thus, it indicates the stability conditions for the most stable Fe-S species. As shown in Figure 2, stoichiometric pyrrhotite (or troilite) and pyrite (denoted by the generic names FEIISPPT and FEIIS2PPT, respectively) are the most stable species. Thus, these species are expected to be formed after an infinitely long equilibration time in their respective domains of E and pH. Troilite is predicted to be stable in weakly acidic, neutral and alkaline solutions ($5.3 < \text{pH} < 13.3$) at reducing conditions. The whole stability area of troilite lies below the H⁺/H₂ equilibrium line (denoted by a), which indicates that its formation will be thermodynamically favored in anoxic environments. Mild oxidation of troilite, consistent with the transformation of S²⁻ into S⁰, will lead to the formation of pyrite as the most stable species containing sulfur in the -2 and 0 oxidation states. In contrast to troilite, pyrite will also be stable in acidic environments. Further oxidation will lead to the dissolution of pyrite in acidic solution (as a result of

oxidizing S_2^{2-} to SO_4^{2-}) or to the formation of iron oxides (as a result of oxidizing Fe^{2+} to Fe^{3+} as well as S_2^{2-} to SO_4^{2-}).

In the second step of our analysis, troilite and pyrite are excluded from the model in order to find which species are next in the order of thermodynamic stability. The result is shown in Figure 3. For clarity, the potential range in Fig. 3 is reduced to (-1, 1) from the (-2, 2) range in Fig. 2 because there is no variation in speciation at potentials above 1 V and below -1 V. As shown in Figure 3, mackinawite would be stable if the formation of troilite was inhibited. Mackinawite appears to be somewhat less stable than troilite in weakly acidic solutions and, therefore, its stability field begins at slightly higher pH values ($pH > 6.2$). At the same time, marcasite is the less stable crystalline form of FeS_2 . If the formation of pyrite was kinetically inhibited, the stability field of marcasite would be practically the same as that of pyrite. In fact, experimental data indicate that the formation of marcasite is kinetically favored under acidic conditions^{6,7}.

In the third step, marcasite is removed while mackinawite is retained in the model. This reveals which iron sulfide species would form as a product of mild oxidation of mackinawite if the formation of both marcasite and pyrite was inhibited. Figure 4 shows that a small, wedge-shaped stability field of greigite appears in this case. Greigite is stable for pH values between approximately 5.9 and 7.4 in a narrow range of electrochemical potentials. In this pH range, mild oxidation of mackinawite would lead to the formation of greigite. It is worthwhile to note that the stability field of greigite lies entirely above the H^+/H_2 equilibrium line (denoted by a) in contrast to the stability fields of pyrite and marcasite, which straddle this line. This indicates that the oxidation of mackinawite to greigite cannot occur in environments, in which the cathodic reaction is the reduction of H^+ to H_2 . The location of the greigite field above the H^+/H_2 line is consistent with the probable mechanism of conversion of mackinawite to greigite by oxidation in the presence of oxygen or by growth of a sulfur sublattice on a mackinawite lattice and a subsequent redistribution of atoms⁵. In the latter case, the sulfur (S^0) would result from the oxidation of S^{2-} , which can occur only at potentials above the H^+/H_2 line. The relative location of the greigite field and the H^+/H_2 line also agrees with the finding of Osseo-Asare and Wei²² that mackinawite does not undergo oxidation in solution in the absence of O_2^0 or S^0 .

In the fourth step, the simulations are run after excluding both mackinawite and greigite in addition to the previously removed pyrite, marcasite and troilite. As shown in Figure 5, amorphous FeS and the $FeHS^+$ ion are the precursor species that would form if the formation of more stable Fe-S compounds was inhibited. Amorphous FeS is stable only in neutral and weakly alkaline environments. In weakly acidic media, $FeHS^+$ is the likely precursor for the formation of more stable sulfides.

Finally, Figure 6 shows the results obtained after removing amorphous FeS in addition to the previously removed species. The $FeHS^+$ ion and siderite ($FeCO_3$) appear as precursors for the iron sulfides. The connection between siderite and the formation of another iron sulfide form, smythite, was pointed out by Rickard²³. However, no thermochemical data are available for smythite and, therefore, this relationship could not be quantitatively evaluated.

All diagrams indicate that the formation of the various iron monosulfides starts at pH values in the vicinity of 5 or 6. This is close to the natural pH of oilfield brines. For example, the calculated pH of a brine with a composition given in Table 2 is 6.5. The pH may vary depending on the H_2S and CO_2 content, concentrations of alkaline components and pressure, which influences the solubility of H_2S and

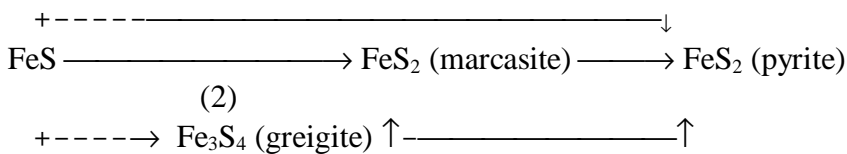
CO₂ in the liquid phase. Thus, the iron sulfides may or may not form depending on the exact composition of the brine.

Figures 2 - 6 make it possible to construct the replacement sequence of the iron sulfides that contain sulfur primarily in the -2 oxidation state (i.e., monosulfides):



The consecutive transitions between amorphous FeS, mackinawite and pyrrhotite are in agreement with experimental data in aqueous solutions^{6,7,23}. Also, there is evidence that the mackinawite → pyrrhotite transformation occurs when iron sulfide scales grow on the surface of iron corroding in H₂S-containing environments (Meyer et al., 1958).

The transformation of these compounds into iron sulfides that contain significant quantities of sulfur in both the -2 and 0 oxidation states involves a certain oxidation process as indicated by higher E ranges on the stability diagrams. The stability diagrams indicate that the following sequences are thermodynamically feasible:



where FeS denotes, in principle, any iron monosulfide form. The above reaction sequences are consistent with the experimental observation that the formation of pyrite in alkaline and near-neutral solutions involves an iron monosulfide precursor.⁵⁻⁷ The stability diagrams do not indicate which FeS form will act as a precursor for FeS₂ formation. In fact, there is experimental evidence that either amorphous FeS³ or mackinawite^{4,6,7} can occur as intermediate forms during pyrite formation from solution. The particular conversion pathway will depend on the conditions in the aqueous system. As shown in Figure 4, the mackinawite → greigite → pyrite transformation is not thermodynamically feasible under strictly reducing conditions because the greigite field lies above the H⁺/H₂ line. This is in agreement with the observations of Schoonen and Barnes⁶⁻⁷ that greigite is not formed in solution under very reducing conditions. The mackinawite → pyrite and mackinawite → marcasite → pyrite transformations are possible under very reducing conditions because both marcasite and pyrite stability fields straddle the H⁺/H₂ line (cf. Figures 2 and 3). This is consistent with experimental observations in solutions⁶⁻⁷.

The replacement sequences (1) and (2) are also confirmed by experimental observations of iron/solution interfaces in H₂S-containing environments. In particular, Meyer et al.¹ found the transformation of mackinawite (described as kansite) into pyrrhotite and, subsequently, pyrite in the corrosion products of Fe in H₂S - containing NaCl solutions. Matsuo and Tominaga²⁴ found mackinawite as a product of corrosion of steel in an atmosphere of nitrogen and hydrogen sulfide. Mackinawite gradually transformed to greigite.

The stability diagrams are significantly influenced by the concentrations of H₂S and iron in the aqueous environment. The stability fields of iron sulfides increase with rising concentrations of H₂S and Fe in the solution. The greigite stability field is particularly sensitive to the H₂S and Fe concentrations.

For example, greigite disappears if the overall H₂S molality drops below ca. $4 \cdot 10^{-4}$ at the Fe²⁺ molality of 10^{-4} mol/kg.

The effect of the concentration of brine components such as NaCl or CaCl₂ on the stability of the various iron sulfides appears to be minor and is not explicitly observed in the diagrams. The effect of pressure is primarily related to the solubility of H₂S in acidic and neutral solutions. Thus, an increase in pressure will somewhat increase the stability areas of various iron sulfides.

H₂S Corrosion Under Gas Pipeline Conditions

After determining the Fe-S species that can be formed as a result of H₂S corrosion, it is worthwhile to use the thermodynamic model to rationalize the results of actual H₂S corrosion experiments. Recently, Lyle²⁵ performed a series of laboratory measurements of CO₂/H₂S corrosion under stagnant or low-flow gas pipeline conditions in the presence or absence of oxygen. In this work, correlations are sought between the observed corrosion rates and the predicted formation of potentially protective iron sulfide scales. As a tool for such analysis, we use the chemical stability diagrams, in which the potential is not used as an independent variable but, rather, results from the equilibrium state in the solution. To determine the conditions that are conducive to the formation of protective FeS layers, the simulations are performed by excluding the species that are not formed as initial corrosion products (i.e., pyrite, marcasite and troilite). Thus, the simulations are focused on the species that form during the initial stages of reactions at the iron/solution interface (i.e., mackinawite, greigite and amorphous FeS^{1,25}).

First, the simulations were carried out for conditions that approximate those in a stagnant solution that is in equilibrium with a large volume of a neutral gas with varying amounts of H₂S, CO₂ and O₂²⁵. Since the experiments were performed in a stagnant solution, a buildup of corrosion products could be expected in the vessel. This should have increased the amount of dissolved Fe that was available for the formation of iron sulfide phases. Therefore, a different kind of stability diagrams is constructed to investigate the effect of dissolved Fe in an explicit way. Figure 7 shows a stability diagram with the molality of Fe in the aqueous phase as an x-axis variable. The y axis shows the amount of H₂S added to the solution per 1 kg of water on the assumption that the vapor phase contains 100 moles of neutral gases. The latter assumption is arbitrary, but it is consistent with the requirement that the amount of the vapor phase should be large so that its composition practically does not change as a result of reactions. The total pressure in the system is 500 psi (34.02 atm) and the temperature is 60 °F (15.56 °C), in agreement with the experimental conditions reported by Lyle²⁵. Under these conditions, the value of 0.1 mol on the vertical axis corresponds to 0.5 psi (0.034 atm) H₂S and the value of 1 corresponds to 5 (0.34 atm) psi H₂S. Further, it is assumed that the system contains 20 psi (1.36 atm) CO₂. An important result that can be observed in Figure 7 is the dependence of the stability field of mackinawite on the amounts of both H₂S and dissolved Fe. Mackinawite starts to appear when the amount of dissolved Fe is quite large, i.e., 10^{-3} for 0.5 psi of H₂S. Thus, a substantial buildup of corrosion products in the aqueous phase is required to stabilize the potentially protective mackinawite phase. Another interesting observation is the boundary between FeCO₃ (siderite) and mackinawite. This boundary shows how much H₂S is necessary to form mackinawite in the presence of CO₂. The limiting partial pressure of H₂S is approximately 0.1 psia, which is fairly low. Thus, siderite is replaced with mackinawite as the concentration of H₂S increases beyond a certain limit.

The next simulation focused on the effects of oxygen in stagnant solutions. The E-pH diagrams discussed above indicate that a rise in the potential, due to the addition of oxygen, may result in the formation of additional solid phases (Fe_2O_3 and/or greigite) or may shift the state of the system in the active dissolution range, where Fe^{2+} is stable. However, the E-pH diagrams are inherently incapable of determining the exact amounts of oxygen that will give rise to these transformations. Therefore, a diagram with the amount of oxygen as an independent variable has been generated.

Figure 8 shows a stability diagram for a system containing 0.5 psia H_2S as a function of the amount of dissolved Fe and O_2 added to the vapor phase. As before, the gas phase is assumed to contain 100 moles of neutral gas per 1 kg of aqueous phase. Therefore, 1 m O_2 on the vertical axis corresponds to 10,000 ppmv O_2 , 0.1 m corresponds to 1,000 ppmv etc.

As shown in Figure 8, the increase in the amount of oxygen results first in the conversion of mackinawite into greigite. This starts at 1 ppmv O_2 (10^{-4} on the vertical scale). The boundary between mackinawite and greigite depends on the amount of dissolved iron. However, mackinawite disappears for oxygen amounts exceeding ca. 50 ppmv for reasonable amounts of dissolved Fe. A further increase in the amount of O_2 results in the dissolution of greigite and a shift of the state of the system to the active dissolution range.

Additionally, Figure 8 shows the values of observed rates of general corrosion that correspond to the experimental concentrations of H_2S and O_2 ²⁵. The corrosion rates are shown in mpy and are enclosed within shaded circles on the diagram. The lowest circle corresponds to the absence of oxygen, which can be identified with 0.1 ppmv O_2 . Based on the experimental conditions, it has been estimated that the total concentration of dissolved Fe reaches approximately $10^{-3.5}$. As expected, the rates are reasonably low in the stability areas of mackinawite and greigite, which are likely to form protective films. As the amount of O_2 increases, the iron sulfides cease to be stable and the corrosion rate increases.

With a small increase in oxygen concentrations, mackinawite is predicted to convert into greigite. It can be expected that the transformation of mackinawite into an incompatible crystal structure of greigite will lead to the disruption of the surface layer and increase corrosion. In fact, there is some experimental evidence for this phenomenon². It may be hypothesized that a porous, incompatible mackinawite/greigite surface may facilitate the initiation of pitting. As shown in Figure 8, the uniform corrosion rates are similar in the stability fields of mackinawite and greigite. However, the experiments of Lyle²⁵ indicate that pitting corrosion can occur with as little as 100 ppmv oxygen in the gas. This is consistent with the hypothesis that a transformation of mackinawite into greigite promotes the initiation of pitting. Thus, the simulations suggest that the minimum oxygen level below which oxygen-induced pitting is not likely varies from 1 to 50 ppmv depending on the amount of dissolved iron.

The stability diagrams are also useful for simulating experiments performed in flowing solutions. In such solutions, the buildup of corrosion products is avoided and the concentrations of components in the aqueous phase remain virtually unchanged. In particular, the pH of the solution can be assumed to be constant rather than vary with the amount of dissolved iron. Thus, stability diagrams for flowing solutions are generated using pH as an independent variable and the amount of dissolved iron as a parameter.

Figure 9 shows the behavior of a system containing 0.5 psia (0.034 atm) H_2S , 10 psi (0.68 atm) CO_2 and 10^{-4} m of dissolved iron as a function of oxygen concentration and pH. It is noteworthy that the

stability fields of mackinawite and greigite depend strongly on pH. At pH values ranging from 6 to 8.5, mackinawite ceases to be stable and converts to greigite at oxygen concentrations as low as 1 ppmv (which corresponds to 10^{-4} on Figure 9). On the other hand, mackinawite is predicted to be much more stable (up to ca. 1000 ppmv O₂) at higher pH values.

Additionally, Figure 9 shows experimental corrosion rates in the liquid phase (cf. the values enclosed within shaded circles). The corrosion rate measurements were performed at pH=6, which is approximately at the edge of the stability fields of mackinawite and greigite. The observed corrosion rates at pH=6 are weakly dependent on the amount of oxygen. This is consistent with the predicted stability diagram because an increase in O₂ concentration from 0 to 1000 ppmv is not accompanied by the creation or disappearance of a protective solid phase. The observed corrosion rates are high. It can be expected that a small shift toward higher pH values should result in a reduction of general corrosion rates because iron sulfides would then become stable.

Conclusions

A program has been developed for the construction of real-solution stability diagrams, which summarize the thermodynamic behavior of heterogeneous solid/aqueous systems in an easy-to-use format. The stability diagrams readily indicate the conditions for the formation of both stable and metastable iron sulfides in realistically modeled brines. The replacement sequence of the Fe-S species appears to be a consequence of their thermodynamic stability and can be predicted on the basis of stability diagrams. The predicted replacement sequence agrees with the available experimental data on iron sulfide formation in solutions and on the surface of corroding iron.

The stability diagrams can be generated with a flexible choice of independent variables. Therefore, they can be constructed to simulate the actual conditions of corrosion experiments. Although thermodynamic models are inherently incapable of predicting corrosion rates, they indicate the conditions for which the corrosion rates are likely to be reduced due to the formation of potentially protective solids. A comparison with experimental data on CO₂/H₂S corrosion reveals that the observed variations in corrosion rate can be explained using the predicted stability of iron sulfides.

References

1. F.H. Meyer, O.L. Riggs, R.L. McGlasson, J.D. Sudbury, J.D., 1958, *Corrosion*, v. 14, no. 2, p.69-75 (1958).
2. M.B. McNeil, B.J. Little, *Corrosion*, v. 46, no. 7, p. 599-600 (1990).
3. R.A. Berner, *Am. J. Sci.*, v. 265, no. 9, p. 773-785 (1967).
4. R.E. Sweeney, I.R. Kaplan, *Econ. Geology*, v. 68, no. 5, p. 618-634 (1973).
5. J.W. Morse, F.J. Millero, J.C. Cornwell, D. Rickard, *Earth Sci. Rev.*, v. 24, no. 1, p.1-42 (1987).
6. M.A.A. Schoonen, H.L. Barnes, *Geochim. Cosmochim. Acta*, v. 55, no. 6, p. 1495-1504 (1991).
7. M.A.A. Schoonen, H.L. Barnes, *Geochim. Cosmochim. Acta*, v. 55, no. 6, p. 1505-1514 (1991).
8. M. Krs, F. Novak, M. Krsova, P. Pruner, Kouklikova, J. Jansa, *Phys. Earth Planet. Inter.*, v. 70,

- no. 3-4, p. 273-287 (1992).
9. A. Anderko, S.J. Sanders and R.D. Young, *Corrosion*, v. 53, no. 1, p. 43-53 (1997).
 10. M. Pourbaix, *Atlas of electrochemical equilibria in aqueous solutions*: Pergamon Press, New York, NY, 644 p. (1966).
 11. OLI Systems Inc., *OLI Software Manual*, Morris Plains, NJ (1996).
 12. J.F. Zemaitis, Jr., D.M. Clark, M. Rafal, N.C. Scrivner, *Handbook of aqueous electrolyte thermodynamics*: AIChE, New York, NY, 852 p. (1986).
 13. M. Rafal, J.W. Berthold, N.C. Scrivner, S.L. Grise, *Models for electrolyte solutions*, in Sandler, S.I., ed., *Models for Thermodynamic and Phase Equilibria Calculations*: M. Dekker, New York, NY, p. 601-670 (1995).
 14. H.C. Helgeson, D.H. Kirkham, G.C. Flowers, *Am. J. Sci.*, v. 281, no. 10, p. 1249-1516 (1981).
 15. J.C. Tanger, H.C. Helgeson, *Am. J. Sci.*, v. 288, no. 1, p. 19-98 (1988).
 16. L.A. Bromley, *AIChE J.*, v. 19, no. 2, p. 313-320 (1973).
 17. K.S. Pitzer, *J. Phys. Chem.*, v. 77, no. 2, p. 268-277 (1973).
 18. G. Soave, *Chem. Eng. Sci.*, v. 27, no. 6, p. 1197-1203 (1972).
 19. M.M. Lencka, E. Nielsen, A. Anderko, R.E. Riman, *Chem. Materials*, v. 9, p. 1116-1125 (1997).
 20. W.M. Latimer, *The Oxidation States of Elements and Their Potentials in Aqueous Solutions*, 2nd Ed.: Prentice-Hall, New York, 392 p. (1952).
 21. O. Kubaschewski, H. Ünal, *High Temp.-High Press.*, v. 9, no. 3, p. 361-365 (1977).
 22. K. Osseo-Asare, D. Wei, *Semiconductor electrochemistry of coal pyrite*, Final Technical Report: Pennsylvania State University, State College, PA, 223 p. (1996).
 23. D.T. Rickard, *Stockholm Contrib. Geol.*, v. 20, no. 4, p. 67-95 (1969).
 24. M. Matsuo, T. Tominaga, *Radiochem. Radioanal. Lett.*, v. 52, no. 3, p. 163-175 (1982).
 25. F.F. Lyle, Jr., *CO₂/H₂S corrosion under wet low-flow gas pipeline conditions in the presence of bicarbonate, chloride and oxygen*. Report for PRC International, Southwest Research Institute, San Antonio, TX, 1997.
 26. E.L. Shock, H.C. Helgeson, *Geochim. Cosmochim. Acta*, v. 52, no. 8, p. 2009-2036 (1988).
 27. E.L. Shock, H.C. Helgeson, *Geochim. Cosmochim. Acta*, v. 54, no. 4, p. 915-943 (1990).
 28. H.P. Meissner, in S.A. Newman, ed., *Thermodynamics of Aqueous Systems with Industrial Applications*: Am. Chem. Soc. Symp. Ser., v. 133, p. 495-511 (1980).
 29. M.W. Chase, C.A. Davies, J.R. Downey, D.J. Frurip, R.A. McDonald, A.N. Syverud, *JANAF thermochemical tables*, 3rd. ed., *J. Phys. Chem. Ref. Data*, v. 14, Supplement No. 1, p. 1-1856 (1985).
 30. D.A. Sverjensky, *Reviews in Mineralogy*, v. 17, p. 177-209 (1987).
 31. D. Wei, K. Osseo-Asare, *J. Colloid Interface Sci.*, v. 174, no. 2, p. 273-282 (1995).

APPENDIX

Thermodynamic Framework

In a multicomponent system, the partial molal Gibbs energy of the i -th species is related to the molality (m_i) by

$$\bar{G}_i = \bar{G}_i^0 + RT \ln m_i \gamma_i \quad (\text{A-1})$$

where \bar{G}_i^0 is the standard-state partial Gibbs energy and γ_i is the activity coefficient. Thus, the thermodynamic properties of the system can be calculated if the standard-state Gibbs energies are available for all species as functions of temperature and pressure (i.e., $\bar{G}_i^0(T, P)$) and the activity coefficients are known as functions of the composition vector \mathbf{m} and temperature (i.e., $\gamma_i(\mathbf{m}, T)$). From basic thermodynamics, the standard-state Gibbs energy of formation $\bar{G}_i^0(T, P)$ can be calculated as a function of temperature and pressure if the following data are available:

- (1) Gibbs energy of formation at a reference temperature and pressure (usually, $T_r = 298.15$ K and $P_r = 1$ bar);
- (2) Enthalpy of formation at T_r and P_r ;
- (3) Entropy at T_r and P_r ;
- (4) Heat capacity as a function of temperature and pressure and
- (5) Volume as a function of temperature and pressure.

The key to representing the standard-state properties over substantial temperature and pressure ranges is the accurate knowledge of the heat capacity and volume. For this purpose, the Helgeson-Kirkham-Flowers¹⁴ equation of state is used. This equation accurately represents the standard-state thermodynamic functions for aqueous, ionic or neutral, species as functions of both temperature and pressure. In its revised form¹⁵, the HKF equation is capable of reproducing the standard-state properties up to 1000 °C and 5 kbar.

The HKF equation is based on the solvation theory and expresses the standard-state thermodynamic functions as sums of structural and solvation contributions, the latter being dependent on the properties of the solvent (i.e., water). The standard partial molal volume (\bar{V}_0) and heat capacity (\bar{C}_p^0) are given by:

$$\bar{V}_0 = a_1 + \frac{a_2}{\Psi + P} + \left(a_3 + \frac{a_4}{\Psi + P} \right) \left(\frac{1}{T - \Theta} \right) - wQ + \left(\frac{1}{e} - 1 \right) \left(\frac{f_w}{fP} \right)_T \quad (\text{A-2})$$

$$\begin{aligned} \bar{C}_p^0 = c_1 + \frac{c_2}{(T - \Theta)^2} - \left(\frac{2T}{(T - \Theta)^3} \right) \left(a_3(P - P_r) + a_4 \ln \frac{\Psi + P}{\Psi + P_r} \right) + wTX + 2TY \left(\frac{f_w}{fT} \right)_p \\ - T \left(\frac{1}{e} - 1 \right) \left(\frac{f_w^2}{fT^2} \right)_p \end{aligned} \quad (\text{A-3})$$

where a_1, a_2, a_3, a_4, c_1 and c_2 represent species-dependent nonsolvation parameters, T_r is the reference temperature of 298.15 K, P_r is the reference pressure of 1 bar, Ψ and Θ refer to solvent parameters equal to 2600 bars and 228 K, respectively, $Q, X,$ and Y denote the Born functions given by

$$Q = \frac{1}{e} \left(\frac{\mathcal{H} \ln e}{\mathcal{H} P} \right)_T \quad (\text{A-4})$$

$$X = \frac{1}{e} \left[\left(\frac{\mathcal{H}^2 \ln e}{\mathcal{H}^2} \right)_P - \left(\frac{\mathcal{H} \ln e}{\mathcal{H}} \right)_P^2 \right] \quad (\text{A-5})$$

$$Y = \frac{1}{e} \left(\frac{\mathcal{H} \ln e}{\mathcal{H}} \right)_P \quad (\text{A-6})$$

where ϵ is the dielectric constant of water and ω stands for the Born coefficient, which is defined for the j -th aqueous species by

$$\mathbf{w}_j \equiv \mathbf{w}_j^{abs} - Z_j \mathbf{w}_{H^+}^{abs} \quad (\text{A-7})$$

In equation (A-7), Z_j is the charge on the j -th aqueous species, $\mathbf{w}_{H^+}^{abs}$ refers to the absolute Born coefficient of the hydrogen ion and \mathbf{w}_j^{abs} designates the absolute Born coefficient of the j -th species given by

$$\mathbf{w}_j^{abs} = \frac{N^0 e^2 Z_j^2}{2r_{e,j}} \quad (\text{A-8})$$

where N^0 is the Avogadro number, e is the electron charge and $r_{e,j}$ denotes the effective electrostatic radius of the j -th species, which is related to the crystallographic radius $r_{x,j}$ by

$$r_{e,j} = r_{x,j} + |z_j| (k_z + g) \quad (\text{A-9})$$

where k_z represents a charge-dependent constant equal to 0.0 for anions and 0.94 for cations and g denotes a generalized function of temperature and density. Thus, the HKF equation expresses the heat capacity and volume as functions of pure water properties and seven empirical parameters, which have been tabulated for large numbers of ions, complexes and neutral, both inorganic and organic, molecules. The remaining thermodynamic properties are obtained by thermodynamic integration using the values of the Gibbs energy, enthalpy and entropy at reference temperature and pressure as integration constants.

If the HKF equation parameters are not available from the regression of experimental data, they can be estimated. For this purpose, Shock and Helgeson²⁶⁻²⁷ presented correlations for most solution species except for complexes. Sverjensky³⁰ developed an estimation method for several classes of complexes. In addition to the HKF equation parameters, these methods make it possible to predict the reference-state enthalpy and entropy if the reference-state Gibbs energy is known. These and other estimation techniques have been reviewed in detail by Rafal et al.¹³

The activity coefficient model used for representing the solution nonideality is an extended form of an expression developed by Bromley.¹⁶ The Bromley equation is a combination of the Debye-Hückel

term for long-range electrostatic interactions and a semi-empirical expression for short-range interactions between cations and anions. In a multicomponent system, the activity coefficient of an ion i is given by

$$\log \mathbf{g} = \frac{-Az_i^2 I^{1/2}}{1 + I^{1/2}} + \sum_j^{NO} \left[\frac{|z_i| + |z_j|}{2} \right]^2 \left[\frac{(0.06 + 0.6B_{ij})|z_i z_j|}{\left(1 + \frac{1.5}{|z_i z_j|} I\right)^2} + B_{ij} + C_{ij} I + D_{ij} I^2 \right] m_j \quad (\text{A-10})$$

where A is the Debye-Hückel coefficient which depends on temperature and solvent properties, z_i is the number of charges on ion i , I is the ionic strength (i.e., $I = 0.5 \sum z_i^2 m_i$), NO is the number of ions with charges opposite to that of ion i , and B_{ij} , C_{ij} and D_{ij} are empirical, temperature-dependent cation-anion interaction parameters. Bromley's original formulation¹⁶ contains only one interaction parameter, B_{ij} , which is sufficient for systems with moderate ionic strength. For concentrated systems, the two additional coefficients C_{ij} and D_{ij} usually become necessary. The three-parameter form of the Bromley model is capable of reproducing activity coefficients in solutions with ionic strength up to 30 mol/kg. The temperature dependence of the B_{ij} , C_{ij} and D_{ij} parameters is usually expressed using a simple quadratic function.

In the absence of sufficient experimental data, reasonable predictions can be made using a method due to Meissner²⁸, which makes it possible to extrapolate the activity coefficients to higher ionic strengths based on only a single, experimental or predicted, data point. Also, the parameter B can be estimated using a correlation with entropies of ions.

The Bromley model is restricted to interactions between cations and anions. For ion-molecule and molecule-molecule interactions, the well-known model of Pitzer¹⁷ is used. Unlike the Bromley model, the Pitzer model is not accompanied by methods for estimating missing parameters. However, most of the solution nonideality can be accounted for by cation-anion interactions, for which the more predictive Bromley model is available.

TABLE 1

Fe-S SPECIES CONSIDERED IN THE CALCULATIONS AND THEIR THERMOCHEMICAL PROPERTIES

Species	Assumed stoichiometry	$\Delta_f G^0 /$ kcal mol ⁻¹	$\Delta_f H^0 /$ kcal mol ⁻¹	$S^0 /$ cal mol ⁻¹ K ⁻¹	$C_p^0 /$ cal mol ⁻¹ K ⁻¹	Reference
Stoichiometric pyrrhotite (troilite)	FeS	-24.37	-24.30	14.42	12.07	29
Pyrite	FeS ₂	-38.26	-41.00	12.65	14.85	29
Marcasite	FeS ₂	-37.32	-40.00	12.87	14.91	29
Mackinawite	FeS	-22.3	-21.9*	15.4*	12.0*	3
Greigite	Fe ₃ S ₄	-69.4	-70.3*	47.1*	42.0*	3
Amorphous FeS	FeS	-21.3	-20.9*	15.4*	12.0*	3
FeHS ⁺	FeHS ⁺	-24.931	-36.5*	-9.0*	29.6*	31

* Estimated values

TABLE 2

COMPOSITION OF A SIMULATED OIL FIELD BRINE (IN 10⁻³ MOL KG⁻¹)

NaCl	CaCl ₂	MgCl ₂	BaCl ₂	NaHCO ₃	Na ₂ SO ₄	H ₂ S	FeCl ₂
513.0	22.5	6.1	0.2	8.2	2.1	4.0	0.1

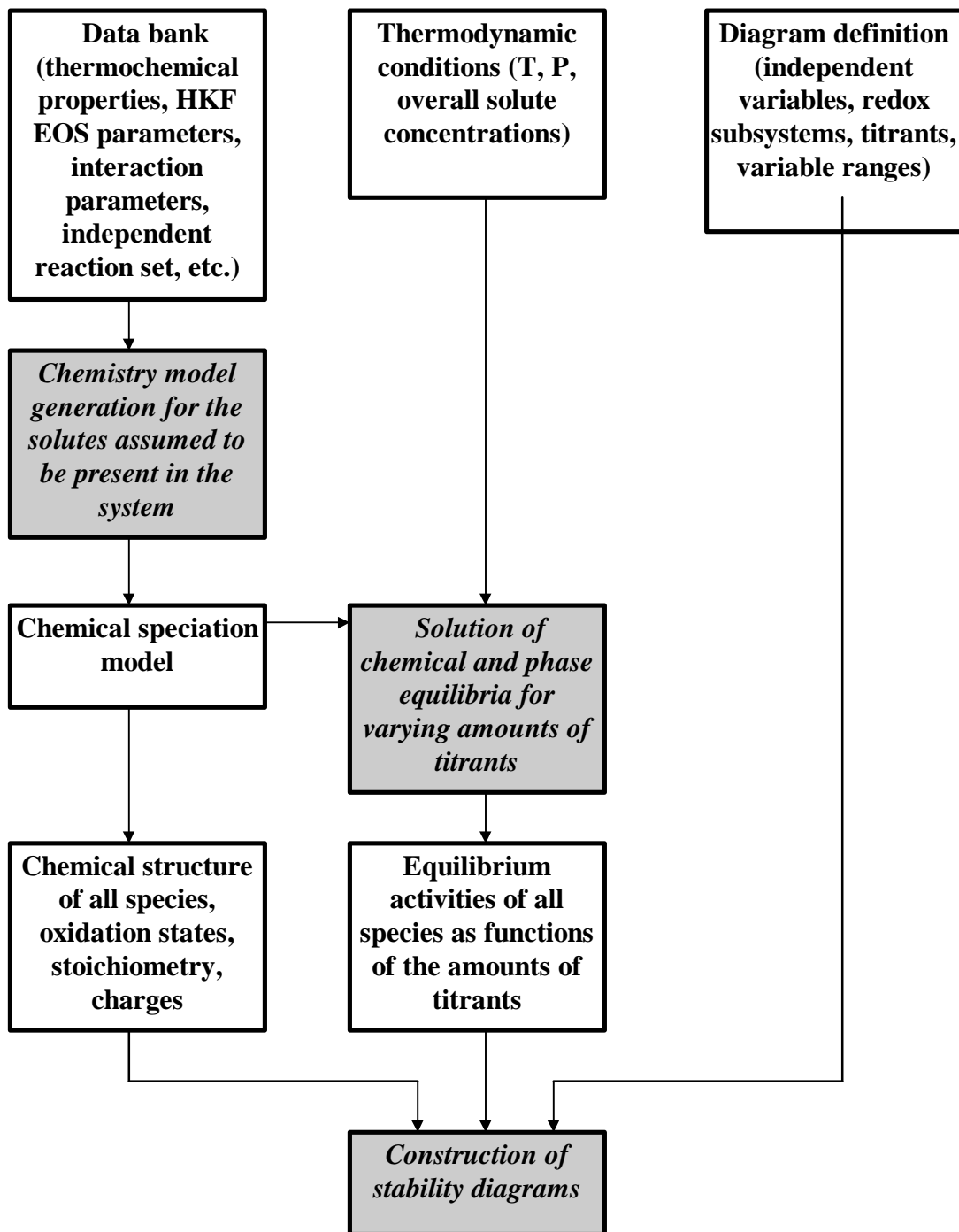


Figure 1. Overall structure of the program for generating stability diagrams.

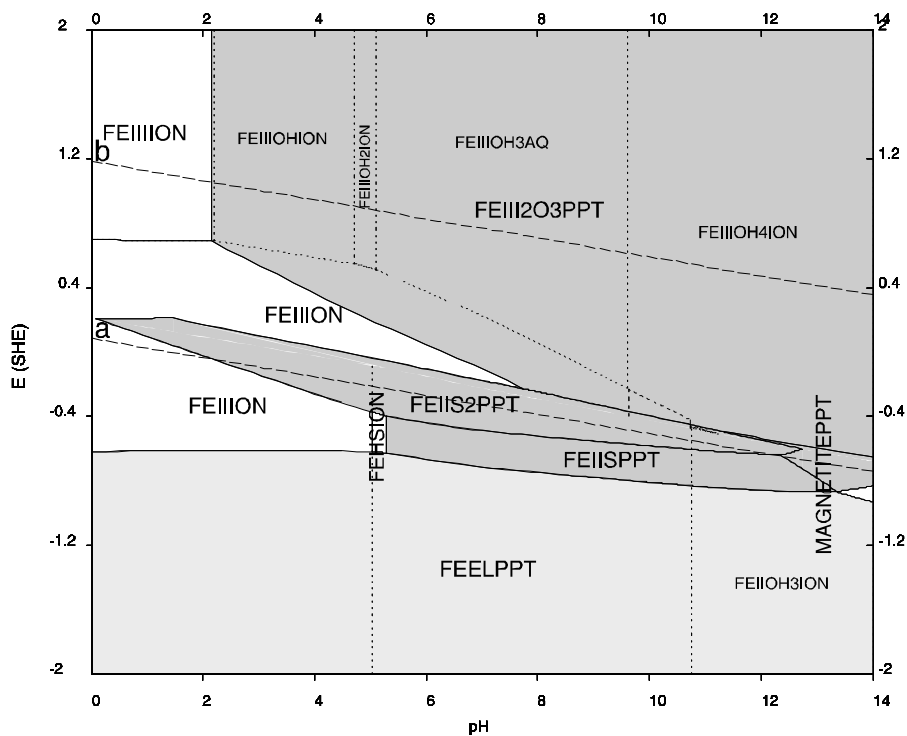


Figure 2. Stability diagram constructed by including all Fe-S species (see Captions).

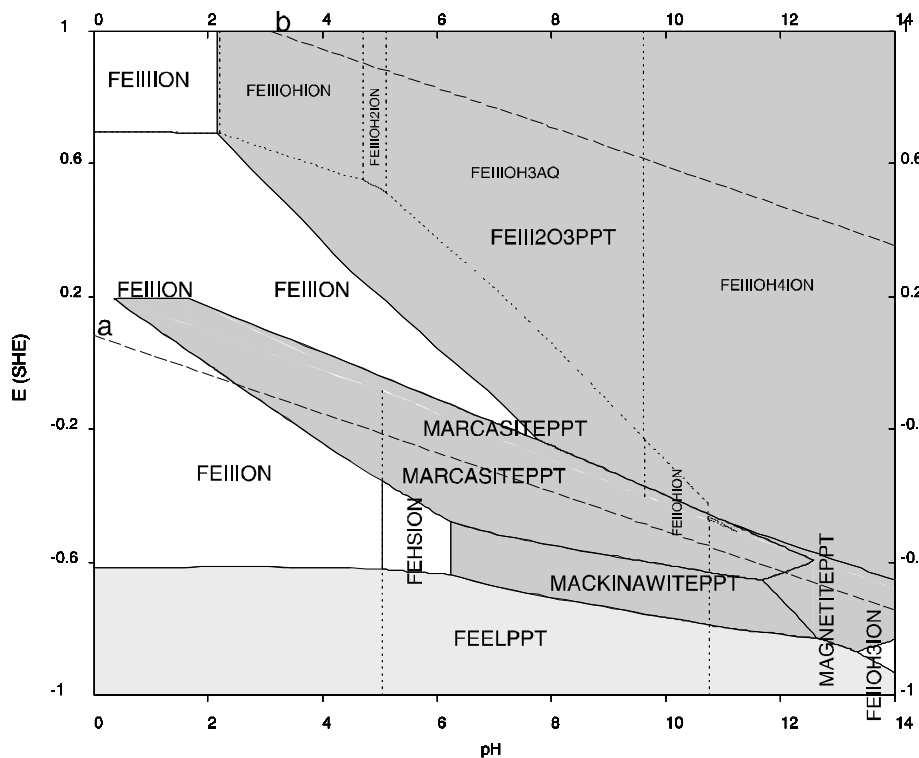


Figure 3. Stability diagram constructed by excluding pyrite (FEIIS2PPT) and troilite (FEIISPT). Marcasite and mackinawite are shown as the metastable iron sulfide species.

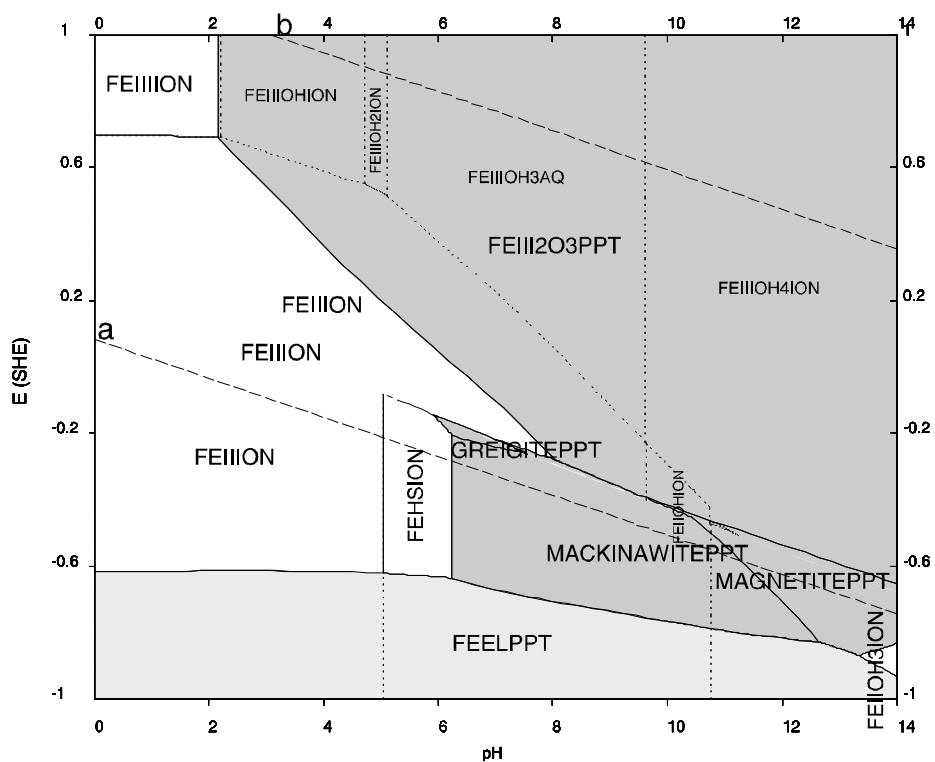


Figure 4. Stability diagram constructed by excluding marcasite in addition to the species excluded in Figure 3. Mackinawite and greigite are shown as the metastable iron sulfide species.

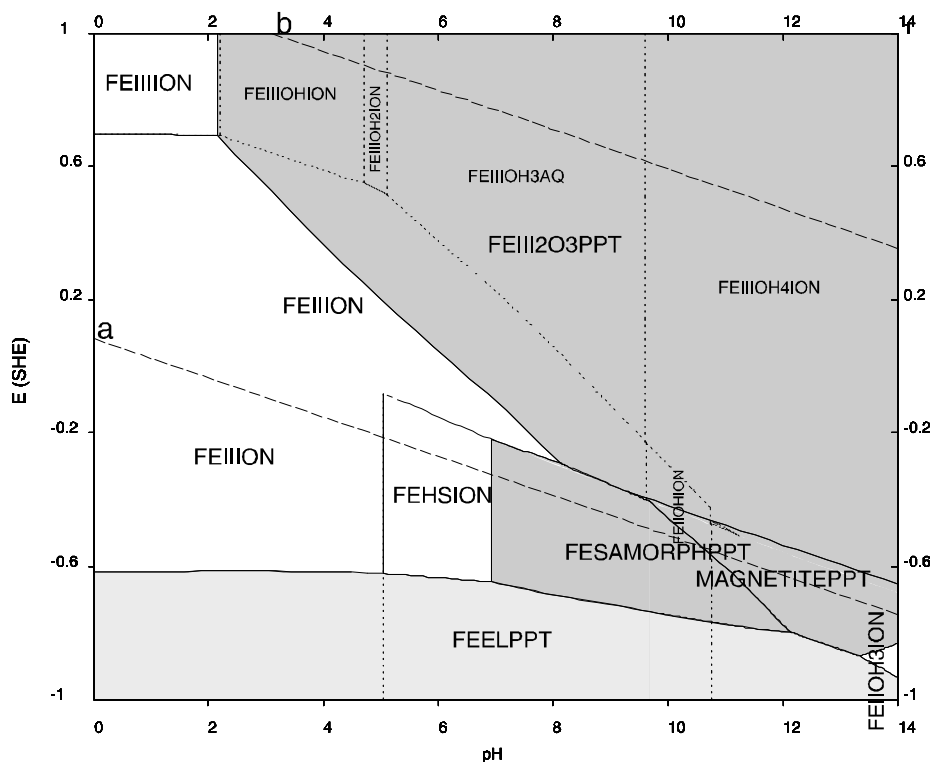


Figure 5. Stability diagram constructed by excluding mackinawite and greigite in addition to the species excluded in Figure 4. Amorphous FeS (i.e., FESAMORPHPPT) is shown as a metastable iron sulfide precursor.

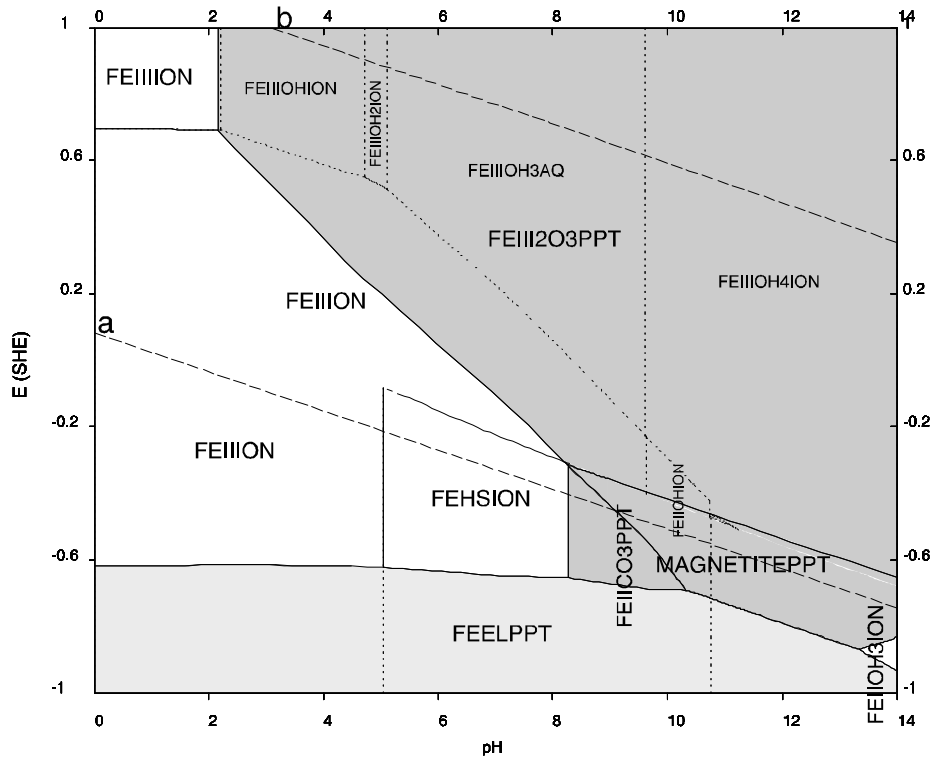


Figure 6. Stability diagram constructed by excluding amorphous FeS in addition to the species excluded in Figure 5. The $FeHS^+$ ion (FEHSION) and iron carbonate (FEIIICO3PPT) are shown as precursors for iron sulfide formation.

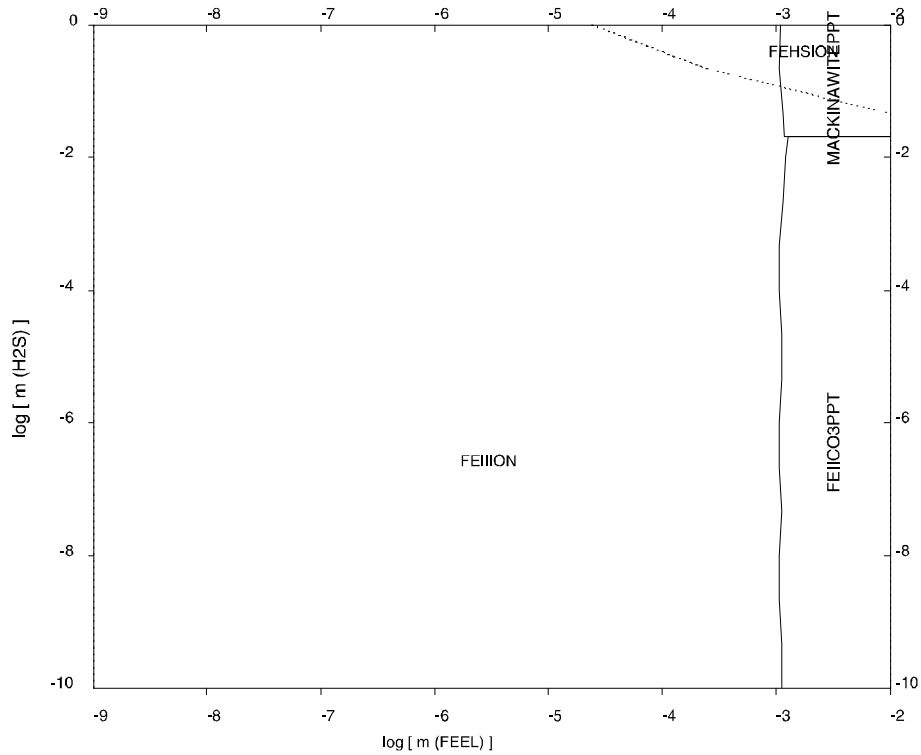


Figure 7. Stability diagram for a system containing 10 psi CO_2 as a function of molality of reacted Fe and the number of moles of H_2S per 1 kg of H_2O and 100 mol of neutral gas phase.

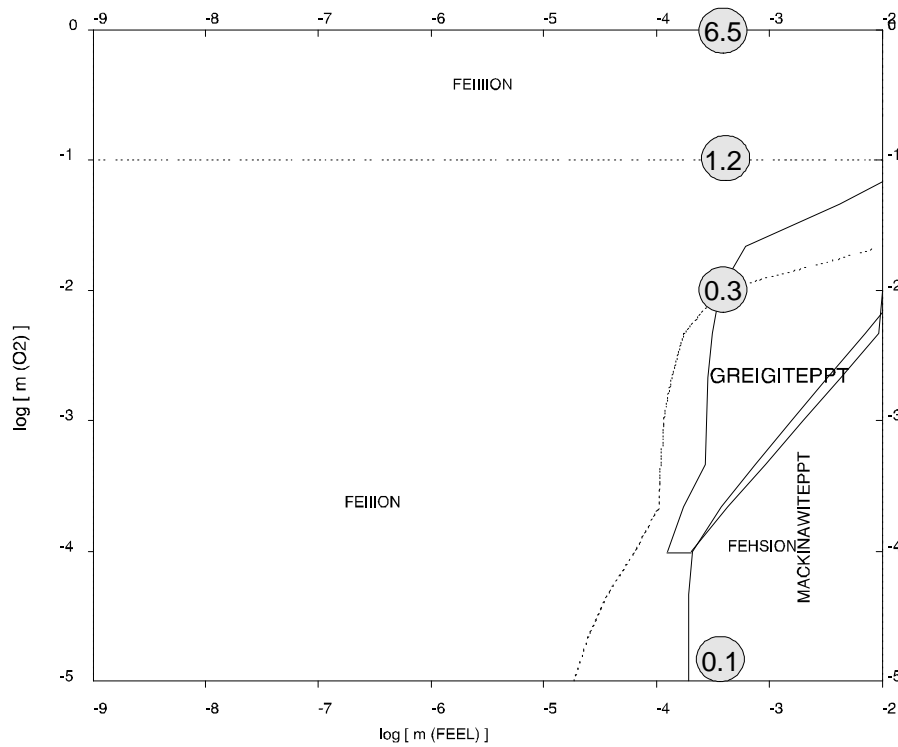


Figure 8. Stability diagram for a system containing 0.5 psi H₂S as a function of Fe and O₂ concentrations. Corrosion rates in mpy²⁵ are shown in shaded circles.

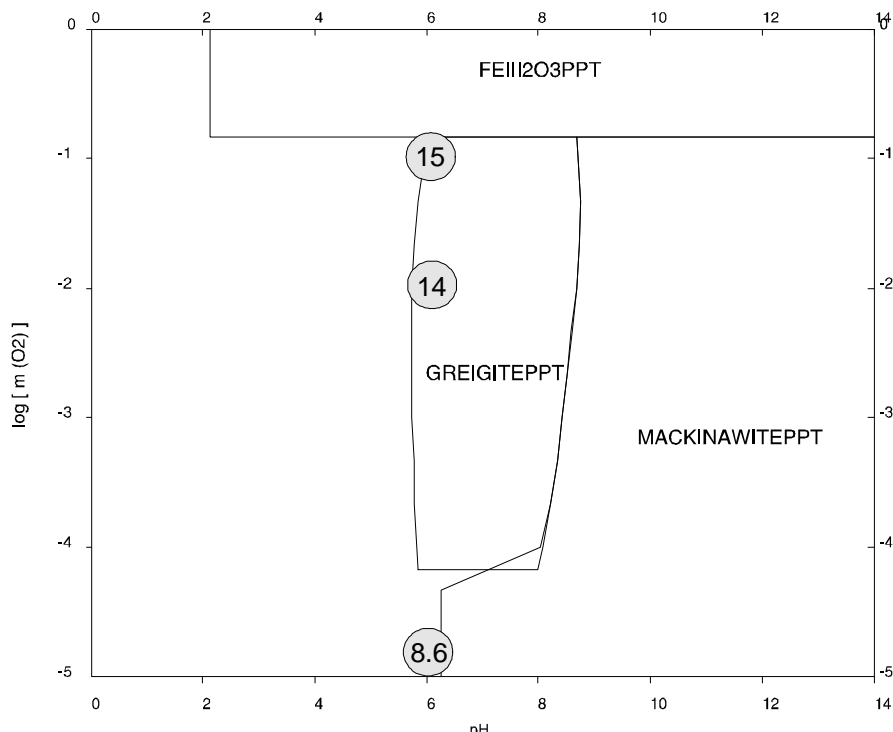


Figure 9. Stability diagram for a system containing 10⁻⁴ m dissolved Fe, 10 psi CO₂ and 0.5 psi H₂S as a function of pH and O₂ amount per 1 kg of H₂O and 100 mol of neutral gas phase. Corrosion rates in mpy²⁵ are shown in shaded circles.

Captions to Figures

Figure 1. Overall structure of the program for generating stability diagrams.

Figure 2. Stability diagram constructed by including all Fe-S species. The stable iron sulfide species are pyrite (denoted by the generic name FEIIS2PPT) and stoichiometric pyrrhotite (or troilite, denoted by FEIISPPT). The symbols FEIIION, FEIIIOHION, FEIIIOH2ION, FEIIIOH3AQ, FEIIIOH4ION, FEII2O3PPT, MAGNETITEPPT, FEIIION, FEHSION, FEIIOHION, FEIIOH3ION and FEELPPT denote Fe^{3+} , FeOH^{2+} , $\text{Fe}(\text{OH})_2^+$, $\text{Fe}(\text{OH})_{3,\text{aq}}$, $\text{Fe}(\text{OH})_4^-$, Fe_2O_3 , Fe_3O_4 , Fe^{2+} , FeHS^+ , FeOH^+ , $\text{Fe}(\text{OH})_3^-$ and $\text{Fe}_{(\text{s})}$, respectively. The dashed lines marked by “a” and “b” represent the H^+/H_2 and $\text{O}_2^0/\text{H}_2\text{O}$ redox equilibria, respectively.

Figure 3. Stability diagram constructed by excluding pyrite (FEIIS2PPT) and troilite (FEIISPPT). Marcasite and mackinawite are shown as the metastable iron sulfide species.

Figure 4. Stability diagram constructed by excluding marcasite in addition to the species excluded in Figure 3. Mackinawite and greigite are shown as the metastable iron sulfide species.

Figure 5. Stability diagram constructed by excluding mackinawite and greigite in addition to the species excluded in Figure 4. Amorphous FeS (i.e., FESAMORHPPT) is shown as a metastable iron sulfide precursor.

Figure 6. Stability diagram constructed by excluding amorphous FeS in addition to the species excluded in Figure 5. The FeHS^+ ion (FEHSION) and iron carbonate (FEIICO3PPT) are shown as precursors for iron sulfide formation.

Figure 7. Stability diagram for a system containing 10 psi CO_2 as a function of molality of reacted Fe and the number of moles of H_2S per 1 kg of H_2O and 100 mol of neutral gas phase.

Figure 8. Stability diagram for a system containing 0.5 psi H_2S as a function of Fe and O_2 concentrations. Corrosion rates in mpy (Lyle, 1997) are shown in shaded circles.

Figure 9. Stability diagram for a system containing 10^{-4} m dissolved Fe, 10 psi CO_2 and 0.5 psi H_2S as a function of pH and O_2 amount per 1 kg of H_2O and 100 mol of neutral gas phase. Corrosion rates in mpy (Lyle, 1997) are shown in shaded circles.